On-chip storage of broadband photonic qubits in a cavity-protected rare-earth ensemble

Tian Zhong,[1] Jonathan M. Kindem,[1] Jake Rochman,[1] and Andrei Faraon[1,*]

[1] *T. J. Watson Laboratory of Applied Physics, California Institute of Technology, 1200 E California Blvd, Pasadena, CA, 91125, USA*

* faraon@caltech.edu

Ensembles of solid-state optical emitters enable broadband quantum storage [1, 2] and transduction of photonic qubits [3, 4], with applications in high-rate optical quantum networks [5] for secure communications [6, 7], global time-keeping [8], and interconnecting future quantum computers. To realize coherent quantum information transfer using ensembles, spin rephasing techniques are currently used to mitigate fast decoherence resulting from inhomogeneous broadening [9, 10]. Here we use a dense ensemble of neodymium rare-earth ions strongly coupled to a nanophotonic resonator to demonstrate that decoherence of a single photon excitation is near-completely suppressed via cavity protection [1, 11] - a new techinique for accessing the decoherence-free subspace of collective coupling. The protected Rabi oscillations between the cavity field and the atomic superradiant state thereby enable ultra-fast transfer of photonic frequency qubits into the ions (∼50 GHz bandwidth), followed by retrieval with 98.7% fidelity. By coupling the superradiant excitation to other long-lived rare-earth spin states, this technology will enable broadband, always-ready quantum memories and fast optical-to-microwave transducers.

Ensembles of rare-earth ions doped in crystals exhibit outstanding quantum coherence properties and broad inhomogeneous linewidths that are suitable for quantum information transfer with fast photons [13]. They are used in state-of-the-art quantum memories both in optical and microwave domain [2, 9, 10, 14–16], and are promising candidates for optical to microwave quantum transduction [3, 4]. One major challenge towards broadband quantum interfaces based on solid-state emitters is that information stored in the collective excitation of the ensemble quickly decoheres because of inhomogeneous broadening. To restore the optical coherence, protocols based on spectral hole burning techniques like atomic frequency comb (AFC) [10, 17, 18] and controlled reversible inhomogeneous broadening (CRIB) [9] have been perfected. Although effective, these protocols involve long (hundreds of miliseconds) and complex preparation procedures that generally limit the interface bandwidth. Recently, it was proposed [1, 11] that ensemble decoherence can be suppressed via strong coupling to a cavity. This phenomenon, called cavity protection, has been experimentally observed, though not in full effect, in the microwave domain with a NV spin ensemble [19]. Here, we demonstrate for the first time strong cavity protection against decoherence in the optical domain using a dense ensemble (a few millions) of neodymium (Nd) atoms coupled

to a nanophotonic cavity. Exploiting the protected mapping of photonic qubits to atomic superradiant excitations, we realize a 50 GHz quantum light-matter interface that could find applications in future quantum networks.

The dynamics of a cavity mode coupled to an atomic ensemble are described by the Tavis-Cummings Hamiltonian [20]. We focus on the interaction term $H_{int} = i\hbar\Omega(S^- a^\dagger - S^+ a)$ where $a^\dagger$ and a are creation and annihilation operators of the cavity mode, and the collective spin operators $S^\pm = \frac{1}{\sqrt{N}} \sum \sigma_k^\pm$ act on N atoms each of frequency ω_k. Ω denotes a collective coupling strength $\Omega^2 = \sum_k^N g_k^2$ which scales up the single atom coupling g_k by $\sqrt{N}$. When the cavity and the ensemble are in resonance, the coupled system exhibits two bright polariton states with equal mix of atomic and photonic components detuned by $\pm\Omega$ from the mean ensemble frequency. The polaritons decay via radiative emission and decohere by coupling to dark subradiant states that overlap spectrally with the ensemble [1, 11, 21]. The dark-state coupling critically depends on the energy separation between the polaritons and the subradiant states, and also on the specific profile of the inhomogeneous spectral distribution $\rho(\omega) = \sum_k g_k^2 \delta(\omega - \omega_k)/\Omega^2$ [1, 11]. In the limiting case of a Lorentzian distribution, considerable damping given by the width of the inhomogeneous broadening persists even with an infinite coupling Ω. When the spectral distribution exhibits a faster-than-Lorentzian decay (e.g. Gaussian), the damping of the coherent Rabi oscillation is diminished at increasing Ω - the system becomes 'cavity protected' as conceptually illustrated in Fig. 1a. In this case, the atomic component of the polariton is purely the symmetric superradiant state [22].

We probe the cavity-protection regime in an optical nanocavity based on our triangular beam design [23, 24] fabricated in 0.1% Nd doped yttrium vanadate (YVO) crystal using focused ion beam (Fig. 1e). The cavity has a fundamental TM mode resonance with measured quality factor of 7,700 ($\kappa/2\pi \sim$44 GHz energy decay rate), a simulated mode volume $V_{\text{mode}} = 1(\lambda/n)^3$=0.063 μm^3, and contains $N \sim 10^6$ ions. The resonance wavelength is 877.1 nm, close to the ${}^4I_{9/2}(Y_1) - {}^4F_{3/2}(Z_1)$ transition of Nd^{3+} at 879.8 nm. The device was cooled down to 3.6 K (Montana Instruments Cryostation) and a magnetic field of 500 mT was applied perpendicular to the YVO c-axis, which enhanced the optical coherence time to T_2=390 ns (measured via photon echoes). The **B** field caused a Zeeman splitting of the Y_1, Z_1 states into 4 levels. For the applied magnetic field orientation, cross-transitions are minimized [25]. Therefore the system can be viewed as two independent distributions

of emitters (Fig. 1b) both coupled to the cavity with similar strengths. To capture the spectral shape of the distribution, a q-Gaussian function was used to fit each transition [19], yielding a shape parameter q=1.01 (1 for Gaussian, 2 for Lorentzian). For simplicity, subsequently we treat the two sub-ensembles as one joint distribution with an effective full-width at half-maximum (FWHM) of $\gamma_q = 2\Delta\sqrt{\frac{2q-2}{2q-2}}$=24 GHz and a parameter Δ=14.6 GHz (2Δ represents the FWHM for a Lorentzian distribution).

To achieve strong coupling, the cavity resonance was red-tuned by gas condensation [23] while the cavity transmission spectra excited by a broadband superluminescent diode was recorded using a spectrometer. In Fig. 2a, a strong anti-crossing is observed. The on-resonance spectrum (Fig. 2b) reveals two polariton peaks with a Rabi splitting of $\Omega_R/2\pi$=48$\pm$2 GHz. The cavity tuning continuously changed the effective collective coupling Ω according to $\Omega = \Omega_0/\sqrt{1+4\delta^2/\kappa^2}$ [23], where $\delta = \omega_c - \omega_a$ is the cavity-ensemble detuning and Ω_0 denotes the maximum collective coupling obtained by fitting the spectrum in Fig. 2b with a known model (Supplementary Information III). The decay rates $\Gamma(\Omega)$ were determined from the FWHM linewidth of the cavity (in the detuned regime) and the polariton peak (in the strong coupling regime). The plot in Fig. 2c corresponds to the left anti-crossing trajectory in Fig. 2a as the cavity shifted from lower wavelengths towards resonance, and the Γ at large Ω was of the lower polariton. Cavity protection manifested as Γ decreased rapidly to a minimum of $\Gamma \sim$22 GHz at maximum coupling. We note the exact reverse trend took place from the right trajectory as the cavity moved away from resonance. The data in Fig. 2c shows excellent agreement with the analytical expression $\Gamma = \kappa/2 + \gamma_h + \pi\Omega^2\rho(\Omega)$ [1] as the red curve, which describes the $\Omega \to \infty$ limit. In our case, the full protection limit is approached by having $\Gamma \sim \kappa/2$. The residual broadening estimated from the $\pi\Omega^2\rho(\Omega)$ term was $\approx$0.1 GHz, more than two orders of magnitude suppressed than without protection. To contrast with the absence of protection, we also plot in green the theoretical decay for a Lorentzian distribution ($\Gamma = \Delta + \kappa/2 \pm \sqrt{(\Delta-\kappa/2)^2 - 4\Omega^2}$) assuming the same Δ, of which $\Gamma(\Omega)$ remains constant even in the strong-coupling limit.

The cavity-protected system acts as a quantum interface where a broadband photon can be transferred to the superradiant atomic excitation. We measure the coherent, ultra-fast transfer dynamics using pulsed excitations of the polariton modes. The experimental setup is depicted in Fig. 1d. A mode-locked Ti:Sapphire laser at 85 MHz repetition rate (Thorlabs Octavius) was filtered to a pulse width of 4 ps using a monochromator, which was sufficient

to simultaneously excite both upper ($|\omega_+\rangle \rightarrow |1\rangle$) and lower ($|\omega_-\rangle \rightarrow |0\rangle$) polaritions. The filtered laser was attenuated and sent through a Michelson setup to produce two pulses with less-than-one mean photon number separated by a variable delay τ that were coupled into the cavity (red path) and the transmitted signal was collected (blue path) for direct detection using a silicon single photon counter. The integrated counts at varying delays produces optical autocorrelation signals revealing the temporal evolution of the polaritons. The mirror at each Michelson arm was interchangeable with a Gires-Tournois Interferometer (GTI) etalon, which generates a $\sim \pi/2$ phase chirp between the two polaritons (Methods). Furthermore, a narrow bandpass filter was optionally inserted in either arm that allowed only one polariton to be excited. This combination enabled a comprehensive polariton excitation scheme that covered individual polariton $|0\rangle$ or $|1\rangle$, and superposition states of two polaritons i.e. $|+\rangle = 1/\sqrt{2}(|0\rangle + |1\rangle)$ or $|\circlearrowleft\rangle = 1/\sqrt{2}(|0\rangle + i|1\rangle)$.

Figure 3 plots the theoretical interference fringe amplitudes along with the measured results for a few representative two-pulse excitation schemes. The mean photon number per pulse coupled in the cavity was estimated at μ=0.5. The case of an uncoupled cavity is plotted in Fig. 3a, showing a fitted decay constant ($4/\kappa$) of ∼14.5 ps. When only one polariton ($|0\rangle$ or $|1\rangle$) was excited, the decay was extended to 29.0 ps as a result of cavity protection (Fig. 3b). For the superposition state $|+\rangle$, Ramsey-like fringes were obtained, revealing extended Rabi oscillations between photonic and atomic excitations beyond the cavity lifetime (Fig. 3c). In the case of Fig. 3d, the system was first driven into $|\circlearrowleft\rangle$ state, and was subsequently excited by a $|+\rangle$ pulse. The resulting fringe showed the Rabi oscillations with the nodes shifted with respect to 3c by about 5.5 ps ($\sim 1/4\tau_R$), in agreement with our theoretical model (Supplementary information III). Those nodes correspond to the quantum excitation being entirely stored in the ensemble with no energy left in the cavity mode, during which time the stored qubit dephases at a significantly slower rate than the inhomogeneous broadening.

This quantum interface is similar to an AFC with two teeth, one at each polariton, that form the basis of a frequency bin qubit as shown in Fig. 4a. Similar to AFC, photons are stored and then released after the inverse of the comb period, which in this case is a Rabi period τ_R. The interface bandwidth is ∼50 GHz, spanning two polaritons, and the qubits are of the form $|0\rangle$, $|+\rangle = 1/\sqrt{2}(|0\rangle + |1\rangle)$ or $|\circlearrowleft\rangle = 1/\sqrt{2}(|0\rangle + i|1\rangle)$. To characterize this process, quantum state tomography on the released qubit after a delay τ_R was performed.

As direct projection measurements were difficult given the high-bandwidth, we adopted an interferometric scheme (Fig. 4b) to assess the input/output fidelity $F = \langle\psi_{in}|\rho_{out}|\psi_{in}\rangle$, where $|\psi_{in}\rangle$ is the input qubit state and ρ_{out} is the density matrix for the retrieved state, from a set of fringe signals including those in Fig. 3 (Methods and Supplementary Information I). The reconstructed density matrices ρ_{out} for $|0\rangle$, $|+\rangle$, and $|\circlearrowleft\rangle$ input states along with their respective fidelities are shown in Fig. 4c. A mean fidelity of 98.7±0.3% is obtained, which significantly surpasses the classical fidelity limit [3] of 74.9±0.04% that takes into account the Poissonian statistics of the coherent input photons (with μ=0.5) and an imperfect but high storage-retrieval efficiency of 25.6±1.2% (Methods) [4, 5]. The estimated fidelities take into account imperfections in the preparation and measurement of the qubit, such as leakage of traveling waves through the cavity and inaccurate phase shift (ideally $\pi/2$) by the GTI etalon. Thus, the high fidelity indicates a robust quantum transfer with a bandwidth that is significantly broader than existing rare-earth-based light-matter interfaces [14, 18]. To highlight the benefit of cavity protection, we also evaluated the qubit fidelity at a delay of $2\tau_R$, which would be equivalent to the case without cavity protection where the qubit would decohere twice as fast. The measured fidelities at $2\tau_R$ dropped to 83% for $|0\rangle$, 70% for $|+\rangle$, and 69% for $|\circlearrowleft\rangle$, which no longer beats the classical fidelity.

While this interface allows for efficient mapping of the photonic qubit to the ensemble, the qubit dissipates at $\kappa/2$ rate. Improvements in the cavity quality factor to state of the art values of Q$\sim 10^6$ would achieve storage for 1 ns (enough for perform 50 Rabi flips). To enable long-term storage like in an AFC-spin-wave memory [17], the qubit can be transferred from the superradiant state excitation to a long-lived spin level by applying a π pulse within τ_R time. Upon recall, another π pulse can transfer the qubit back to the polariton states and then a cavity photon. For faithful spin-wave storage, the Rabi frequency of the π pulses should exceed the polariton linewidths, which is attainable given the strong light confinement in current nanobeam devices. Compared to existing AFC-spin-wave memories, this interface would not require any preparation steps, thus it is always ready. Taking advantage of on-chip technologies also enable other proposals for long-lived memories in the cavity-protected regime by fast detuning of the cavity-ensemble coupling [1]. Most notably, the cavity-protected mapping of a photonic qubit to a collective superradiant state could compliment the reported coupling of rare-earths to a superconducting resonator [30] to fulfil efficient quantum transduction between optical and microwave photons via Zeeman

or hyperfine transitions in rare-earth ensembles [3, 4].

Methods

Nanocavity design and characterization. The triangular nanobeam has a width of 770 nm and length of 15 μm. 40 periodic subwavelength grooves of 185 nm along the beam axis were milled on top of the nanobeam. The grooves extend across the entire width of the beam, which eases the alignment during fabrication. The period of the grooves were modulated at the center of the beam to form defect modes in the photonic bandgap. The fundamental TM mode, with side, top and cross-section views shown in Fig. 1c, is chosen because it aligns with the strongest dipole of the 879.8 nm transition in Nd:YVO. The theoretical quality factor is 300,000 with a mode volume of $1(\lambda/\mathrm{n})^3$ [24]. Transmission of the nanocavity was measured by vertically coupling free-space input into the nanobeam via a 50x objective lens and a 45°-angled reflector milled into the sample surface, and the cavity output was collected via the other reflector which sent the light back vertically to free space. The output signal was effectively isolated from the input reflections or other spurious light by spatial filtering using a pin hole. When the cavity is on resonance, we measured a total transmission (from free-space input to output) of 20%, which was primarily limited by the imperfect coupling into the nanobeam. The output signal also contained leakage travelling waves (5%) due to finite extinction of the photonic bandgap and other spurious reflections in the system.

Polariton excitation and frequency qubit preparation. The GTI etalon was made of a 250 μm thick quartz slide with backside coated with a gold film. The front side was not coated, which has a reflectivity of 4%. This etalon produces a nearly linear dispersion of 4π/nm over a free spectral range of 0.5 nm near 880 nm. After the GTI etalon, the transform-limited laser pulse acquired a phase chirp, which excited a mixed polariton state approximated by $|0\rangle + e^{i\phi}|1\rangle$, where ϕ is the phase shift over the Rabi splitting. For our custom made etalon, $\phi \approx 0.52\pi$ and the corresponding polarition state was close to $(|0\rangle + i|1\rangle)$.

Quantum state tomography based on two-pulse interferometry. The electric field operators for the two consecutive photonic states $|\psi_1\rangle, |\psi_2\rangle$ coupled to the cavity are written as $\hat{E}_1(t) = \alpha_1 e^{-i\omega_- t}\hat{a_-} + \beta_1 e^{-i\omega_+ t}\hat{a_+}$ and $\hat{E}_2(t) = \alpha_2 e^{-i\omega_- t}\hat{a_-} + \beta_2 e^{-i\omega_+ t}\hat{a_+}$, respectively. For simplicity, we drop the finite linewidth of each polariton mode. The field operator at the single photon detector is $\hat{E}(t) = \hat{E}_1(t-\tau_R) + \hat{E}_2(t)$ corresponding to the first photon delayed

by τ_R after storage in the ensemble, which interferes with the second photon. The count rate on the detector is $C = \langle E(t)^\dagger E(t)\rangle = 2 + 2\cos(\phi)|\alpha_1\alpha_2^* + \beta_1\beta_2^*|$, where ϕ is the phase difference between the two photon wavepackets. This gives interference fringes with an amplitude $A = C_0|\alpha_1\alpha_2^* + \beta_1\beta_2^*|$ as labelled in Fig. 3c, where C_0 is a constant factor set by the input photon number, system transmission and decay rates, and detection efficiencies. By encoding a set of four basis states (Pauli tomography basis) on the second photon, i.e. $\alpha_2|0\rangle + \beta_2|1\rangle$, we construct the set of experimental amplitude parameters $A_j, j = 0...3$ (A_0 for $|\psi_2\rangle = 1/\sqrt{2}|\psi_1\rangle$; A_1 for $|\psi_2\rangle = |+\rangle$, A_2 for $|\psi_2\rangle = |\circlearrowleft\rangle$; A_3 for $\psi_2\rangle = |0\rangle$) which are directly analogous to the set of projection measurement outcomes for calculating the density matrix $\hat{\rho}_{out}$ (see Supplementary Information for detailed derivations)

$$\hat{\rho}_{out} = \frac{1}{2}[\hat{I} + ((A_1/A_0)^2 - 1)\hat{\sigma}_1 + ((A_2/A_0)^2 - 1)\hat{\sigma}_2 + ((A_3/A_0)^2 - 1)\hat{\sigma}_3.] \quad (1)$$

where $\hat{I}$ is the identity operator and $\hat{\sigma}_{1,2,3}$ are the Pauli spin operators. Then we perform a maximal likelyhood estimation [2] to obtain a physical density matrix, which is used to calculate the fidelity $F = \langle\psi_{in}|\hat{\rho}_{out}|\psi_{in}\rangle$

Qubit storage and retrieval efficiency. The storage efficiency is defined as the probability that a photon in the cavity mode is transferred to a collective excitation in the ensemble. This storage efficiency is intrinsically 100% as the polariton modes under cavity protection condition are maximally entangled states between the cavity and the superradiant state. The retrieval efficiency is defined by the number of photons emitted at the cavity output during the second Rabi period (grey window in Fig. 4b) vesus the total transmitted photons. Based on the temporal distribution of the transmitted photons (deconvolved from the oscillation signal in Fig. 3c), the integrated counts during the second Rabi period (grey window in Fig. 4b) was 25.6±1.2% of the total transmitted photons. Note that this storage and retrieval efficiency does not take into account the input coupling and scattering loss. Including the 20±2% transmission efficiency through the device, the overall system efficiency was 5.1±0.7%. The corresponding classical bound for qubit storage fidelity would be 78.9±0.05%, still significantly below the measured fidelities in Fig. 4c.

References

[1] Northup, T. E. & Blatt, R. Quantum information transfer using photons. *Nature Photon.* **8,** 356-363 (2014).

[2] Lvovsky, A. I., Sanders, B. C., & Tittel, W. Optical quantum memory *Nature Photon.* **3,** 706-714 (2009).

[3] Williamson, L. A., Chen, Y.-H., & Longdell, J. J. Magneto-optic modulator with unit quantum efficiency. *Phys. Rev. Lett.* **113,** 203601 (2014).

[4] O' Brien, C., Lauk, N., Blum, S., Morigi, G., & Fleischhauer, M. Interfacing superconducting qubits and telecom photons via a rare-earth-doped crystal. *Phys. Rev. Lett.* **113,** 063603 (2014).

[5] Kimble, H. J. The quantum internet. *Nature* **453,** 1023-1030 (2008).

[6] Xie, Z., *et al.* Harnessing high-dimensional hyperentanglement through a biphoton frequency comb. *Nature Photon.* **9,** 536-542 (2015).

[7] Zhong, T., *et al.* Photon-efficient quantum key distribution using time-energy entanglement with high-dimensional encoding. *New J. Phys.* **17,** 022002 (2015).

[8] Kómár, P., Kessler, E. M., Bishof, M., Jiang, L., Sørensen, A. S., Ye, J., & Lukin, M. D. A quantum network of clocks. *Nature Phys.* **10,** 582-587 (2014).

[9] Hedges, M. P., Longdell, J. J., Li, Y. & Sellars, M. J. Efficient quantum memory for light. *Nature* **465,** 1052-1056 (2010).

[10] de Riedmatten, H., Afzelius, M., Staudt, M. U., Simon, C., & Gisin, N. A solid-state light-matter interface at the single-photon level. *Nature* **456,** 773-777 (2008).

[11] Kurucz, Z., Wesenberg, J. H. & Mølmer, K. Spectroscopic properties of inhomogeneously broadened spin ensembles in a cavity. *Phys. Rev. A* **83,** 053852 (2011).

[12] Diniz, I. *et al.* Strongly coupling a cavity to inhomogeneous ensembles of emitters: Potential for long-lived solid-state quantum memories. *Phys. Rev. A* **84,** 063810 (2011).

[13] Thiel, C., Böttger, T., & Cone, R. Rare-earth-doped materials for applications in quantum information storage and signal processing. *J. Luminesc.* **131,** 353-361(2011).

[14] Tittel, W., Afzelius, M., Chaneliére, T., Cone, R. L., Kröll, S., Moiseev, S. A., & Sellars, M. Photon-echo quantum memory in solid state systems. *Laser & Photon. Rev.* **4,** 244-267 (2010).

[15] Zhong, M., Hedges, M. P., Ahlefeldt, R. L., Bartholomew, J. G., Beavan, S. E., Wittig, S. M., Longdell, J. J., & Sellars, M. J. Optically addressable nuclear spins in a solid with a six-hour

coherence time. *Nature* **517** 177-180 (2015).

[16] Wolfowicz, G. *et al.* Coherent Storage of Microwave Excitations in Rare Earth Nuclear Spins. *Phys. Rev. Lett.* **114,** 170503 (2015).

[17] Afzelius, M. *et al.* Demonstration of Atomic Frequency Comb Memory for Light with Spin-Wave Storage. *Phys. Rev. Lett.* **104,** 040503 (2010).

[18] Saglamyurek, E., *et al.* Broadband waveguide quantum memory for entangled photons. *Nature* **469,** 512-515 (2011).

[19] Putz, S. *et al.* Protecting a spin ensemble against decoherence in the strong-coupling regime of cavity QED. *Nature Phys.* **10,** 720-724 (2014).

[20] Tavis, M., & Cummings, F. W. Exact solution for an N-molecule-radiation-field Hamiltonian. *Phys. Rev.* 170, 379-384 (1968).

[21] Houdré, R., Stanley, R. P., & Ilegems, M. Vacuum-field Rabi splitting in the presence of inhomogeneous broadening: Resolution of a homogeneous linewidth in an inhomogeneously broadened system. *Phys. Rev. A* **53,** 2711-2715 (1996).

[22] Dicke R. H. Coherence in spontaneous radiation processes. *Phys. Rev.* **93,** 99-110 (1954).

[23] Zhong, J. Kindem, J. Miyazono, E., & Faraon, A. Nanophotonic coherent light-matter interfaces based on rare-earth doped crystals. *Nature Commun.* **6,** 8206 (2015).

[24] Zhong, T., Rochman, J. Kindem, J. Miyazono, E., & Faraon, A. High quality factor nanophotonic resonators in bulk rare-earth doped crystals. *Opt. Express* **24,** 536-544 (2016).

[25] Afzelius M. *et al.* Efficient optical pumping of Zeeman spin levels in Nd^{3+}:YVO_4, *J. Luminescence* **130,** 1566-1571 (2010).

[26] Massar, S. & Popescu, S. Optimal extraction of information from finite quantum ensembles. *Phys. Rev. Lett.* **74,** 1259-1263 (1995).

[27] Specht, H. P., Nölleke, C., Reiserer, A., Uphoff, M., Figueroa, E., Ritter, S., & Rempe, G. *Nature* **473,** 190 (2011).

[28] Gündogan, M., Ledingham, P. M., Almasi, A., Cristiani, M., & de Riedmatten, H. Quantum storage of a photonic polarization qubit in a solid. *Phys. Rev. Lett.* **108,** 190504 (2012).

[29] James, D. F. V., Kwiat, P. G., Munro, W. J., & White A. G. Measurement of qubits. *Phys. Rev. A* **64,** 052312 (2001).

[30] Probst, S., Rotzinger, H., Wünsch, S., Jung, P., Jerger, M., Siegel, M., Ustinov, A. V., & Bushev, P. A. Anisotropic Rare-Earth Spin Ensemble Strongly Coupled to a Superconducting

Resonator. *Phys. Rev. Lett.* **110,** 157001 (2013).

Acknowledgements

This work is funded by NSF CAREER 1454607, NSF Institute for Quantum Information and Matter PHY-1125565 with support from Gordon and Betty Moore Foundation GBMF-12500028, and AFOSR Quantum Transduction MURI FA9550-15-1-002. Device fabrication was performed in the Kavli Nanoscience Institute with support from Gordon and Betty Moore Foundation.

Author contributions

A.F. and T.Z. conceived the experiments. T.Z. J. R fabricated the device. T.Z., J.M.K. performed the measurements. T.Z. and J.M.K. analyzed the data. T.Z. and A.F. wrote the manuscript with input from all authors.

Competing financial interests

The authors declare no competing financial interests.

On-chip storage of broadband photonic qubits in a cavity-protected rare-earth ensemble: Supplementary Information

S1. Construction of qubit density matrix from interference fringes of two photons

The state of an arbitrary qubit $|\psi\rangle = \alpha|0\rangle + \beta|1\rangle$, where $|\alpha|^2 + |\beta|^2 = 1$, can be determined by taking a set of four projection measurements represented by the operators $\hat{\mu_0} = |0\rangle\langle 0| + |1\rangle\langle 1|$, $\hat{\mu_1} = |+\rangle\langle +|$, $\hat{\mu_2} = |\circlearrowleft\rangle\langle\circlearrowleft|$, $\hat{\mu_3} = |0\rangle\langle 0|$ [2]. The outcome of these measurements are

$$n_j = C\mathrm{Tr}\{\hat{\rho}\hat{\mu_j}\}, \tag{2}$$

where $\rho = |\phi\rangle\langle\phi|$ for a pure state and the scaling factor C is the number of detected photons, which will be set to 1 in the following derivation. We explicitly write out the four n_j values for an arbitrary qubit as

$$\begin{aligned} n_0 &= 0.5(|\alpha|^2 + |\beta|^2) = 0.5 \\ n_1 &= 0.5|\alpha + \beta|^2 \\ n_2 &= 0.5|\alpha - i\beta|^2 \\ n_3 &= |\alpha|^2. \end{aligned} \tag{3}$$

From these values, the four Stokes parameters are calculated as

$$\begin{aligned} S_0 &= 2n_0 \\ S_1 &= 2(n_1 - n_0) \\ S_2 &= 2(n_2 - n_0) \\ S_3 &= 2(n_3 - n_0). \end{aligned} \tag{4}$$

The density matrix $\hat{\rho}$ is then constructed from the Stokes parameters by

$$\hat{\rho} = \frac{1}{2}\sum_{j=0}^{3}\frac{S_j}{S_0}\hat{\sigma}_j, \tag{5}$$

where $\hat{\sigma}_0$ is the identity operator $\hat{I}$ and $\hat{\sigma}_{1,2,3}$ are the Pauli spin operators.

Now we turn to the measurement of interference between two photonic states represented by the electric field operators $\hat{E}_1(t) = \alpha_1 e^{-i\omega_- t}a_- + \beta_1 e^{-i\omega_+ t}a_+$ and $\hat{E}_2(t) = \alpha_2 e^{-i\omega_- t}a_- + \beta_2 e^{-i\omega_+ t}a_+$, where ω_-, ω_+ are the optical frequencies of the lower and upper polaritons, respectively, with frequency difference $\omega_+ - \omega_- = \Omega_R$. For simplicity, we do not include

the finite linewidth of each polariton as it does not affect the results of the tomography measurement. The field operator at the single photon detector is $\hat{E}(t) = \hat{E}_1(t-\tau_R) + \hat{E}_2(t)$ corresponding to the first photon delayed by τ_R after storage in the ensemble. The count rate on the detector is

$$\begin{aligned} C &\propto \langle E(t)^\dagger E(t)\rangle \\ &= 2 + 2\cos\phi|\alpha_1\alpha_2^* + \beta_1\beta_2^* e^{-i\Omega_R\tau_R}| \\ &= 2 + 2\cos\phi|\alpha_1\alpha_2^* + \beta_1\beta_2^*|, \end{aligned} \tag{6}$$

where the last equality holds for $\Omega_R\tau_R = 2\pi$. Here ϕ is the carrier phase difference between the two photons, which is varied from 0 to 2π to produce interference fringes with a peak-to-peak amplitude $C_{\max} - C_{\min} = 4|\alpha_1\alpha_2^* + \beta_1\beta_2^*|$. We define a set of experimentally measurable fringe amplitude parameters $A = C_0|\alpha_1\alpha_2^* + \beta_1\beta_2^*|$, where C_0 is a constant factor representing the integrated counts. These parameters closely resemble the projection measurement outcomes in Eq. (1) (different by a power of 2) depending on the states encoded on the second photon, i.e. $\alpha_2|0\rangle + \beta_2|1\rangle$. For instance, if we encode the second photon in the same qubit as the first photon but attenuate the intensity by a factor of 2 , i.e. $\alpha_2 = \alpha_1/\sqrt{2}$, $\beta_2 = \beta_1/\sqrt{2}$, we get the amplitude $A_0 = \frac{C_0}{\sqrt{2}}(|\alpha_1|^2 + |\beta_1|^2)$. For $\alpha_2 = \beta_2 = 1/\sqrt{2}$, $A_1 = C_0/\sqrt{2}|\alpha_1 + \beta_1|$. For $\alpha_2 = -i\beta_2 = 1/\sqrt{2}$, $A_2 = C_0/\sqrt{2}|\alpha_1 - i\beta_1|$. For $\alpha_2 = 1$, $\beta_2 = 0$, $A_3 = C_0|\alpha_1|$. Based on the four amplitude values, we construct an equivalent set of Stokes parameter S_j^A

$$\begin{aligned} S_0^A &= 2A_0^2 \\ S_1^A &= 2A_1^2 - 2A_0^2 \\ S_2^A &= 2A_2^2 - 2A_0^2 \\ S_3^A &= 2A_3^2 - 2A_0^2, \end{aligned} \tag{7}$$

from which the density matrix is calculated by

$$\begin{aligned} \hat{\rho} &= \frac{1}{2}\sum_{j=0}^{3} \frac{S_j^A}{S_0^A}\hat{\sigma_j} \\ &= \frac{1}{2}[\hat{I} + ((A_1/A_0)^2 - 1)\hat{\sigma}_1 + ((A_2/A_0)^2 - 1)\hat{\sigma}_2 + ((A_3/A_0)^2 - 1)\hat{\sigma}_3]. \end{aligned} \tag{8}$$

Then we perform a maximal likelyhood estimation [2] to obtain a physical density matrix, which is used to calculate the fidelity $F = \langle\psi_{in}|\hat{\rho}|\psi_{in}\rangle$

S2. Classical storage fidelity for weak coherent photons

The classical fidelity for any storage device measures the best input/output fidelity one can achieve using a classical method. For a given photon number of the input state N_{ph}, the maximum classical fidelity is known to be $F = \frac{N_{ph}+1}{N_{ph}+2}$ [3]. For an input pulse that is in a coherent state with a mean photon number μ, the Poissonian statistics give a N-photon probablity of $P(N_{ph}) = e^{-\mu}\frac{\mu^{N_{ph}}}{N_{ph}!}$. Accounting for each N-photon component, the classical fidelity of a coherent state then is

$$F = \sum_{N_{ph}\geq 1}^{\infty} \frac{N_{ph}+1}{N_{ph}+2}\frac{P(N_{ph})}{1-P(0)} \tag{9}$$

In addition, for an imperfect memory with storage and retrieval efficiency $\eta < 1$, the classical fidelity would be higher because a classical memory can preferentially measure the higher photon component of the input and send out a new qubit. We follow the strategy in [4, 5] that there exists a threshold photon number $N_{\min}$ that the classical memory sends out a qubit when the input photon number is greater than this value, which happens with a probability $1-p$. Otherwise the memory sends out a result for input photon $N_{\min}$ with probability p. Combing the two cases, the memory efficiency is expressed as

$$\eta = \frac{p + \sum_{N_{ph}\geq N_{\min+1}} P(N_{ph})}{1-P(0)} \tag{10}$$

For a given μ and η, the value of $N_{\min}$ can be readily calculated according to [5],

$$N_{\min} = \min\, i : \sum_{N_{ph}\geq i+1} P(N_{ph}) \leq (1-P(0))\eta, \tag{11}$$

which is used to obtain the final classical fidelity

$$F_{\text{class}} = \frac{\frac{N_{\min}+1}{N_{\min}+2}p + \sum_{N_{ph}\geq N_{\min+1}} \frac{N_{ph}+1}{N_{ph}+2}P(N_{ph})}{\eta(1-P(0))} \tag{12}$$

S3. Simulation of the dynamics of the coupled cavity-ensemble system

The model of the system follows that presented in [1] and consists of a cavity mode a of frequency ω_0 coupled with strength g_k to a distribution of N two-level emitters described by modes b_k. We define the cavity frequency ω_0 to be the origin and label the frequency of each emitter as ω_k. We account for the atomic dephasing rate γ and label the cavity field decay as κ. Using the standard input-output formalism [1] for a two sided cavity with input field

c_{in}, reflected field c_r, and transmitted field c_t gives the Heisenberg equations for the system:

$$\begin{aligned}
\dot{a} &= -\left[\frac{\kappa}{2} + i(\omega_0 - \omega)\right] a - \sqrt{\frac{\kappa}{2}} c_{in} + \sum_k g_k b_k \\
\dot{b}_k &= -\left[\frac{\gamma}{2} + i(\omega_k - \omega)\right] b_k - g_k a \\
c_t &= \sqrt{\frac{\kappa}{2}} a \\
c_r &= c_{in} + \sqrt{\frac{\kappa}{2}} a.
\end{aligned}$$

By solving this set of equations in the steady state, we arrive at the complex transmission of the cavity:

$$t(\omega) = \frac{\langle c_t \rangle}{\langle c_{in} \rangle} = \frac{-\frac{\kappa}{2i}}{\omega_0 - \frac{i\kappa}{2} - \omega - \sum_k \frac{g_k^2}{\omega_k - \frac{i\gamma}{2} - \omega}}. \tag{13}$$

For a large number of emitters, we can define the distribution of emitters in terms of a continuous spectral density $\rho(\omega) = \sum_k \frac{g_k^2 \delta(\omega - \omega_k)}{\Omega^2}$. Here Ω is the collective coupling strength defined by $\Omega^2 = \sum_k g_k^2$. The continuum form of the transmission is then [1]

$$t(\omega) = \frac{-\frac{\kappa}{2i}}{\omega_0 - \frac{i\kappa}{2} - \omega - \Omega^2 \int \frac{\rho(\omega') d\omega'}{\omega' - \omega + \frac{i\gamma}{2}}}. \tag{14}$$

In the case of a decoupled cavity ($\Omega = 0$), this reduces to a Lorentzian with full-width at half maximum (FWHM) of $\kappa/2\pi$. From the transmission of the far-detuned cavity, we measure $\kappa/2\pi = 44$ GHz. The measured distribution of atoms $\rho(\omega)$ is described by a q-gaussian with q≈1 and FWHM of 24 GHz. We measure $\gamma = 1/\pi T_2 = 0.82$ MHz using two-pulse photon echoes. Fitting the on-resonance transmission spectrum with these known parameters allows us to determine the collective coupling strength $\Omega = 25$ GHz.

To simulate the dynamics of the system (Fig. 3 theoretical plots and Fig. 4b), we start from the discrete form of the differential equations. In this case, simulating the entire system entails solving a set of $N \sim 10^6$ coupled differential equations. To make the problem more computationally tractable, we instead solve the system of $N_{sim} \ll N$ coupled emitters with frequencies randomly assigned according to the experimentally measured frequency distribution. The coupling strength of each emitter is set as $g = \Omega/\sqrt{N_{sim}}$ such that the collective coupling strength is held constant at the experimentally measured value. This reduced set of equations was then solved numerically in Mathematica using the built-in differential equation solver (NDSolve). The number of simulated emitters was increased until the solution converged (i.e. until increasing the number of simulated emitters no

longer had an effect on the solution). All emitters were assumed to start in the ground state in an empty cavity. The cavity and probe were assumed to be on resonance with the center of the emitter spectral distribution. The input field consisted of two 4 ps pulses separated by variable time τ. The amplitude of the integrated interference (corresponding to the measurement) for each value of τ was determined by integrating the cavity response over the simulation time (10 cavity lifetimes).

References

[1] Diniz, I. *et al.* Strongly coupling a cavity to inhomogeneous ensembles of emitters: Potential for long-lived solid-state quantum memories. *Phys. Rev. A* **84,** 063810 (2011).

[2] James, D. F. V., Kwiat, P. G., Munro, W. J., & White A. G. Measurement of qubits. *Phys. Rev. A* **64,** 052312 (2001).

[3] Massar, S., & Popescu, S. Optimal Extraction of Information from Finite Quantum Ensembles. *Phys. Rev. Lett.* **74,** 1259 (1995).

[4] Specht, H. P., Nölleke, C., Reiserer, A., Uphoff, M., Figueroa, E., Ritter, S., & Rempe, G. *Nature* **473,** 190 (2011).

[5] Gündogan, M., Ledingham, P. M., Almasi, A., Cristiani, M., & de Riedmatten, H. Quantum storage of a photonic polarization qubit in a solid. *Phys. Rev. Lett.* **108,** 190504 (2012).

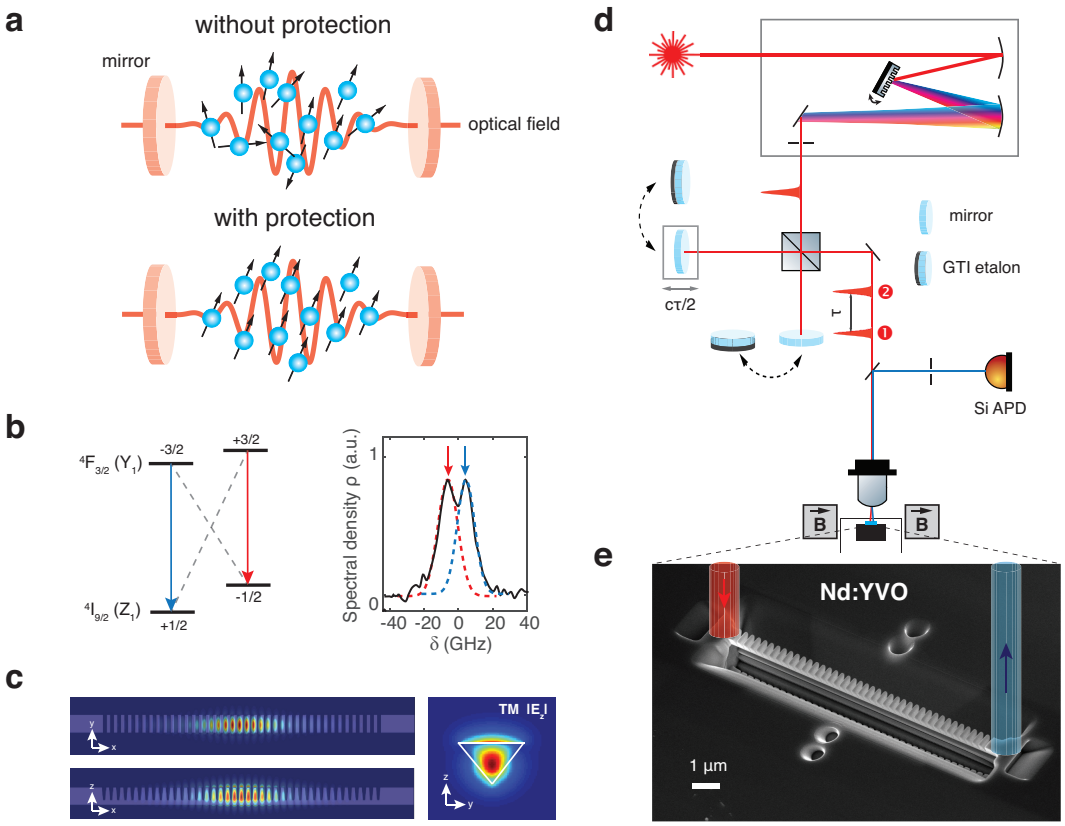

Figure 1. Schematics of the experimental system. **a,** Conceptual illustration of cavity protection for an ensemble of atoms coupled to a cavity mode. Without protection, the collective excitation undergoes dephasing given by the inhomogeneous linewidth. When the cavity protection is in full effect, the collective superandiant excitation is free of such dephasing. Arrow directions represent the phasor of each atomic dipole. **b,** Energy level diagram and possible transitions (dotted lines are forbidden) for Nd in a magnetic field (left). Measured absorption showing two Zeeman split sub-ensembles (right). The red and blue dotted curves are the fit based on a q-Gaussian function with extracted q ∼1.0. The effective FWHM of the entire distribution is 24 GHz. **c,** Simulated TM resonance mode profiles of the triangular nanobeam resonator. **d,** Experimental setup for probing the device. Two attenuated pico-second pulses with controllable delay are generated from a mode-locked laser by frequency filtering and passing through a Michelson setup. The mirrors in each arm of the Michelson interferometer were interchangeable with a custom made GTI etalon to modify the phase chirp of the pulses. The two pulses were transmitted through the cavity and the transmission signal was integrated on a Si APD photon counter. (e) Scanning electron microscope image of the device and schematics of input and output optical signals.

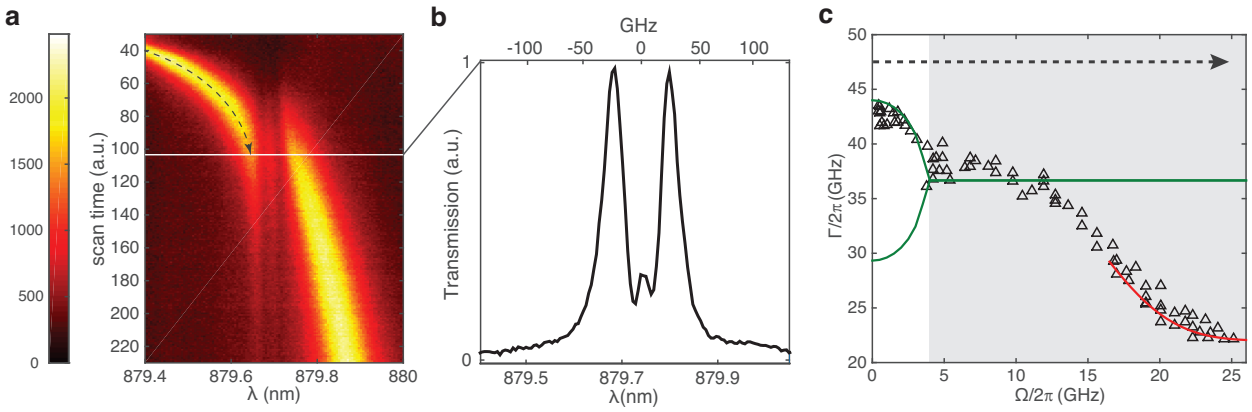

Figure 2. **Cavity protection of the Nd ensemble against decoherence. a,** Cavity transmission spectra while tuning its resonance across the inhomogeneous Nd transition. **b,** On-resonance transmission spectrum showing two polaritons under the strong-coupling condition. **c,** Experimental steady state decay rate extracted from the left anti-crossing trajectory (dotted arrow indicating direction of increasing Ω) in **a** as a function of coupling strength. For strong coupling, Γ decreases rapidly with increasing Ω showing protection of the collective excitation against decoherence. Red curve plots the analytical form of $\Gamma = \kappa/2 + \gamma_h + \pi\Omega^2\rho(\Omega)$ in the very strong coupling regime. Green curve shows the characteristic decay assuming a Lorentzian distribution of the ensemble. The grey background indicates the system entering the strong-coupling (Non-Markovian) regime

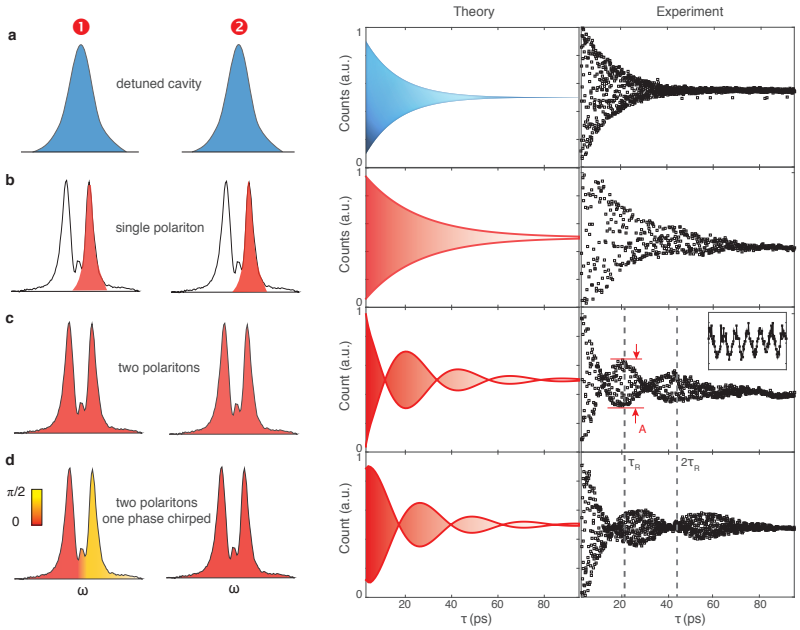

Figure 3. **Time-domain interferometric measurements of the cavity transmission.** Left panels show the cavity transmission spectra for the two pulses under different excitation schemes. Blue area is for uncoupled cavity; red for excited polariton states: yellow for the polarition with a shifted phase. The colored areas were plotted against the polariton spectrum (solid curve). **a,** Simulated and measured cavity decay (i.e. lifetime) when uncoupled from the atoms. **b,** Decay of singly excited lower (upper) polarition (i.e. $|0\rangle(|1\rangle)$). **c,** Decayed oscillations when both polaritons were excited with transform-limited pulses. **d,** Decayed and time-shifted oscillations when two polaritons were initially excited with a $\pi/2$ phase difference (i.e. $|0\rangle + i|1\rangle$) by the first pulse and in phase by the second pulse. **b-d** shows extended decays about twice in **a**, confirming a nearly full protection against ensemble-induced decoherence. The dotted lines mark multiples of Rabi periods τ_R. The inset shows a few fine fringes scaned around τ_R.

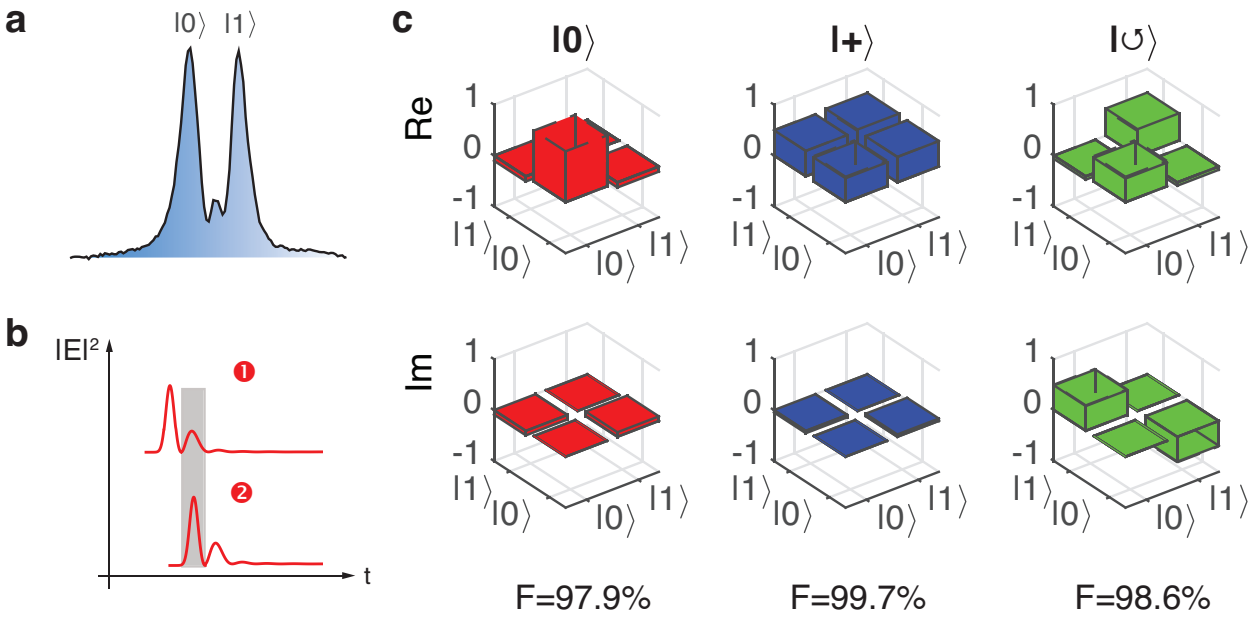

Figure 4. Broadband qubit transfer to the protected Nd ensemble. a, Two polaritons serve as eigen basis for a frequency bin qubit. A phase chirp can be added to construct a generic qubit $|0\rangle + e^{i\phi}|1\rangle$. **b,** Simulated time-domain evolution of the cavity field intensities of two qubit-encoded photons, showing temporal overlap between the retrieved photon from the ensemble ($|\psi_1\rangle$) and the second photon ($|\psi_2\rangle$) directly transmitted through the cavity at time τ_R. The fields dominantly overlap within a temporal window (grey area) when interference occurs yielding integrated photon counts proportional to the overlap $|\langle\psi_2|\psi_1\rangle|$. The overlap after the grey window was negligibly small due to fast cavity decays. **c,** Reconstructed density matrices for each input qubit (top row) delayed by τ_R showing high fidelities.